

Metallic supercurrent field-effect transistor

Giorgio De Simoni,¹ Federico Paolucci,¹ Paolo Solinas,² Elia Strambini,¹ and Francesco Giazotto^{1,*}

¹NEST, Istituto Nanoscienze-CNR and Scuola Normale Superiore, I-56127 Pisa, Italy

²SPIN-CNR, Via Dodecaneso 33, 16146 Genova, Italy

In their original formulation of superconductivity, the London brothers predicted [1] the exponential suppression of an *electrostatic* field inside a superconductor over the so-called London penetration depth, λ_L [2–4]. Despite a few experiments indicating hints of perturbation induced by electrostatic fields [5–7], no clue has been provided so far on the possibility to manipulate metallic superconductors via field-effect. Here we report field-effect control of the supercurrent in *all-metallic* transistors made of different Bardeen-Cooper-Schrieffer (BCS) superconducting thin films. At low temperature, our field-effect transistors (FETs) show a monotonic decay of the critical current under increasing electrostatic field up to total quenching for gate voltage values as large as $\pm 40\text{V}$ in titanium-based devices. This *bipolar* field effect persists up to $\sim 85\%$ of the critical temperature ($\sim 0.41\text{K}$), and in the presence of sizable magnetic fields. A similar behavior was observed in aluminum thin film FETs. A phenomenological theory accounts for our observations, and points towards the interpretation in terms of an electric-field-induced perturbation propagating inside the superconducting film. In our understanding, this affects the pairing potential and quenches the supercurrent. These results could represent a groundbreaking asset for the realization of an *all-metallic* superconducting field-effect electronics and leading-edge quantum information architectures [8, 9].

A generic scheme of our all-metallic supercurrent FETs is displayed in Fig. 1a. The transistors have been fabricated by electron-beam lithography and evaporation of titanium (Ti) or aluminum (Al) on top of an p^{++} -doped Si substrate covered by a 300-nm-thick SiO_2 insulating layer (see Methods Summary for further details). Back and side gate voltages, denoted by V_b and V_s , respectively, are used to generate the electrostatic field that controls the supercurrent flow in the wire. Figure 1b shows a pseudo-color scanning electron micrograph of a typical device. The Ti FET consists of a wire of length $l = 900\text{nm}$, width $w = 200\text{nm}$, and thickness $t = 30\text{nm}$. Similar transistors with length up to a $3\mu\text{m}$ have shown the same behavior. From the critical temperature $T_c \simeq 410\text{mK}$ [see Fig. 1c showing the wire resistance (R) vs temperature (T) characteristic (blue line)] we determined the zero-temperature BCS energy gap, $\Delta_0 = 1.764k_B T_c \simeq 62\mu\text{eV}$, where k_B is the Boltzmann constant. With this parameter, and from the low-temperature normal-state resistance of the wire, $R_N \simeq 45\Omega$, we deduced the London penetration depth, $\lambda_L = \sqrt{\hbar R_N w t / (\pi \mu_0 l \Delta_0)} \simeq 900\text{nm}$ where μ_0 is the vacuum magnetic permeability, and the superconducting coherence length $\xi_0 = \sqrt{\hbar l / (R_N w t N_F e^2 \Delta_0)} \simeq 100\text{nm}$ where $N_F \simeq$

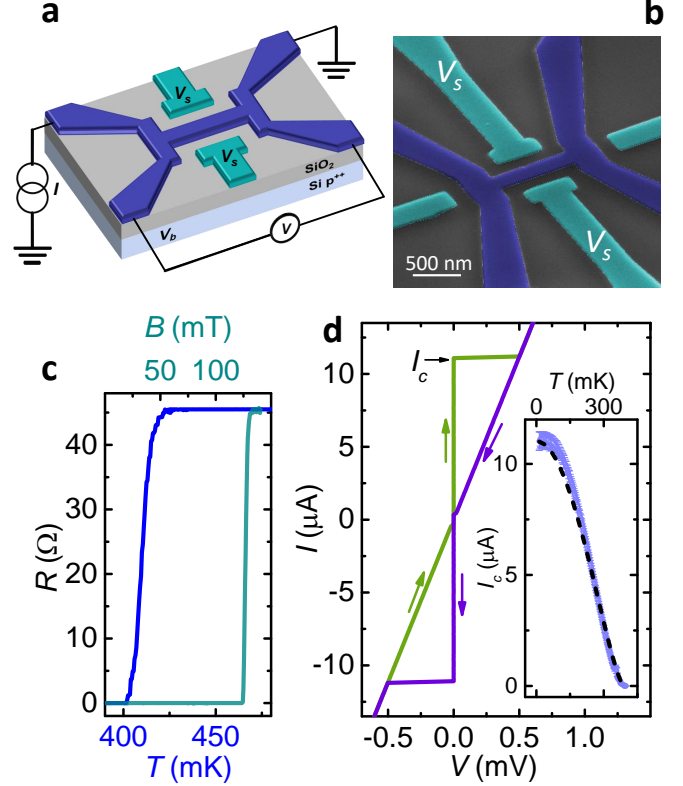


FIG. 1. **The metallic supercurrent field-effect transistor: pre-characterization.** **a**, Schematic of the *all-metallic* supercurrent FET. Back and side gate voltage denoted with V_b and V_s , respectively, are used to control the amplitude of the Ti wire critical supercurrent. V_b is applied to the p^{++} Si substrate. In four-probe measurements, an electric current I is fed into the superconducting wire whereas the voltage drop V is simultaneously recorded as a function of the applied gate voltage. **b**, Pseudo-color scanning electron micrograph of a representative Ti supercurrent FET. The wire length is 900 nm while the width is 200 nm, and the thickness is 30 nm. The transistor core is shown in blue whereas the Ti side gates are colored in cyan. **c**, Resistance R vs temperature T (blue line, bottom horizontal axis), and R vs perpendicular-to-plane magnetic field B at 5 mK (light blue line, top horizontal axis) characteristics of the supercurrent FET. The normal-state resistance of the device is $R_N \sim 45\Omega$. **d**, FET I vs V characteristic measured at 5 mK of bath temperature. $I_c \simeq 11\mu\text{A}$ denotes the wire switching critical current, corresponding to $\sim 1.8 \times 10^5 \text{Acm}^{-2}$ current density consistent with Ti in this temperature range [11]. The inset shows the full temperature evolution of I_c , and its quenching at the critical temperature ($T_c \sim 410\text{mK}$). Dashed line is the prediction of Ref. [11]. The error bars represent the standard deviation of the critical current I_c calculated over 50 measurements.

$1.35 \times 10^{47} \text{J}^{-1} \text{m}^{-3}$ is the density of states at the Fermi level of Ti and e is the electron charge. Since $w, t \ll \lambda_L$, the super-

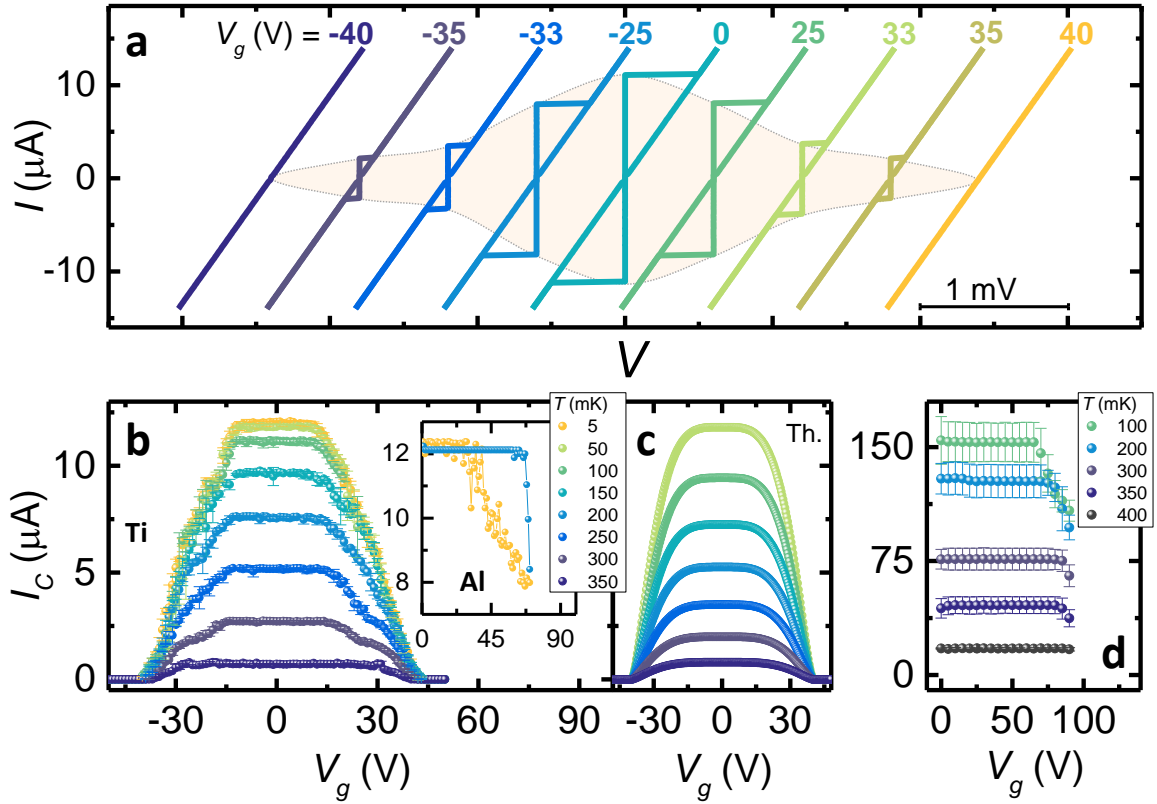


FIG. 2. **Electrostatic-field dependence of the supercurrent FET.** **a**, Current-voltage ($I-V$) characteristics of a Ti supercurrent FET measured at 5 mK for several values of the applied gate voltage ($V_g \equiv V_b = V_s$). Hatched area is a guide to the eye emphasizing the monotonic suppression of the critical current I_c down to zero by increasing $|V_g|$. When the supercurrent vanishes, the $I(V)$ characteristics coincide with that in the normal state, independently of the value of the applied gate voltage. The curves are horizontally offset for clarity. **b**, Behavior of the critical current I_c vs V_g measured at different bath temperatures T . Note the full suppression of I_c occurring for $|V_g| \gtrsim 40$ V. This threshold voltage turns out to be almost independent of bath temperature. The inset shows the $I_c(V_g)$ characteristics for a supercurrent transistor made of aluminum (Al) at two different bath temperatures. Here, the switching current is as large as $\approx 12.3 \mu\text{A}$, corresponding to $\approx 3.7 \times 10^6 \text{Acm}^{-2}$ current density in Al [11, 12]. Note that the different shape of the $I_c(V_g)$ curves in Ti and Al might be related to a different temperature evolution of the electrostatic screening in the two superconducting materials. **c**, Phenomenological critical current I_c vs V_g characteristics calculated with an *ad hoc* model based on Ginzburg-Landau formalism for the same values of bath temperature as in panel b. We emphasize the agreement with the experimental data provided by the model, both for the monotonic decay of the $I_c(V_g)$ characteristics and for the temperature independence of the threshold voltage (V_g^c) over which full suppression of I_c occurs. **d**, I_c vs V_g characteristics measured at different bath temperatures T of a $4 \mu\text{m} \times 4 \mu\text{m}$ Ti FET showing electrostatic field-tuning of the critical current occurring in a large (with respect to λ_L and ξ_0) superconducting structure. In this case, the maximum achieved I_c relative reduction is around $\sim 30\%$ at 100 mK. Here, the electrostatic field was applied only through the back gate ($V_g \equiv V_b$). A critical temperature $T_c \approx 470$ mK, and a perpendicular-to-plane magnetic critical field $B_c \approx 115$ mT are the main characteristic parameters of the Ti film realizing this FET. The error bars in panel b and d represent the standard deviation of the critical current I_c calculated over 50 and 20 measurements, respectively.

conductor can be uniformly penetrated by external magnetic fields [12]. Figure 1c displays the wire R vs perpendicular-to-plane B characteristic at 5 mK (light blue line) revealing a magnetic critical field as large as ~ 127 mT.

Below T_c , dissipationless charge transport occurs in the transistor through Cooper pairs supercurrent. The wire current-voltage ($I-V$) characteristics recorded at 5 mK is shown in the main panel of Fig. 1d. In particular, a switching critical current with amplitude $I_c \approx 11 \mu\text{A}$ is observed displaying an hysteretic behavior which might stem from heating induced in the wire while switching from the resistive to the dissipationless regime [10]. The monotonic decay of I_c as a

function of temperature, and its full quenching at T_c is shown in the inset of Fig. 1d along with the phenomenological prediction by Bardeen (dashed line), $I_c(T) = I_c^0 [1 - (T/T_c)^2]^{3/2}$ where I_c^0 is the zero-temperature, zero-gate voltage wire critical current [11].

Investigation of field effect in our system is performed by current biasing the superconducting wire, and by measuring the critical current vs gate voltage (V_g) applied simultaneously to the back and side gates so that $V_b = V_s \equiv V_g$ (see Fig. 1a). This gate bias configuration maximized the impact of the electric field on I_c . Figure 2a shows the transistor $I-V$ characteristics measured at 5 mK for increasing values of $|V_g|$.

The critical current is monotonically reduced by increasing V_g , and is fully suppressed at a critical voltage $|V_g^c| \simeq 40\text{V}$. At a first glance, this I_c behavior might resemble the one achieved in semiconductor-based Josephson FETs (JoFETs) [8, 9, 13–16] though our transistors are fully *metallic* so that the electric field does not affect the $I - V$ characteristic when the wire switches into the normal state. Yet, in contrast to semiconductor-based JoFETs, the effect is also *bipolar*, i.e., symmetric in the polarity of V_g . The experimental evidence of I_c reduction and quenching seems to point towards the interpretation in terms of a field-effect-induced deformation and suppression of the superconducting pairing potential in the wire, and is the hallmark of the impact of a static electric field on a metallic superconducting film.

The full temperature dependence of field effect in the Ti transistor is shown in Fig. 2b that displays the I_c vs V_g characteristics for several bath temperatures. By increasing T the critical current plateau widens whereas, at the same time, the critical voltage V_g^c determining full suppression of I_c is almost temperature independent. Notably, field effect persists up to about $\sim 85\%$ of T_c , i.e., $\sim 350\text{mK}$, and proves the impact of the electric field on I_c occurring even at higher temperatures.

Analogous behavior was also observed in supercurrent FETs made of thin film aluminum (Al), and consisting of a wire of length $l = 800\text{nm}$, width $w = 30\text{nm}$, and thickness $t = 11\text{nm}$. Key parameters of these structures are a normal-state resistance $R_N \simeq 320\Omega$, a critical temperature $T_c \simeq 1.5\text{K}$, a London penetration depth $\lambda_L \simeq 310\text{nm}$, and a coherence length $\xi_0 \simeq 63\text{nm}$ (see SI). The Al FETs were realized without side gates so that only a back gate $V_g \equiv V_b$ is used to control I_c . The inset of Fig. 2b displays the I_c vs V_g characteristics at two selected bath temperatures. Specifically, a monotonic suppression of I_c from $\simeq 12.3\mu\text{A}$ at $V_g = 0$ down to $\simeq 8\mu\text{A}$ for $V_g = 70\text{V}$ (corresponding to a relative suppression of the order of $\sim 35\%$) is achieved at the lowest temperature. At 200mK the threshold voltage for I_c suppression moves towards larger values. Field effect in Al wires is observed up to $\sim 600\text{mK}$, i.e., around 40% of T_c (see also SI). The similar phenomenology obtained also in Al FETs suggests that these effects might be intrinsic to any metallic superconducting film.

To exclude any possible role of the substrate on the observed phenomena we have fabricated similar Ti FETs on several SiO_2 commercial wafers produced by different manufacturers (both doped and undoped), and sapphire substrates, without noting any substantial difference in the FETs behavior (see SI). Moreover, any hot spot mechanism due to direct charge injection into the wire can be ruled out as the main driving principle for I_c suppression due to the incompatibility with the bipolarity of the effect, and the independence of the critical temperature on gate voltage. In addition, a possible electron field emission mechanism can be excluded as well since it is usually expected to occur for electric fields much larger than the ones applied in the experiment.

A simplified description of the I_c behavior in our system can be obtained through a phenomenological model developed within the Ginzburg-Landau formalism [17] (see SI for

details). According to our model, the wire critical current can be written as

$$I_c(T, V_g) = I_c^0 \left(1 - \frac{T}{T_c}\right)^{3/2} \left[1 - \left(\frac{V_g}{V_g^c}\right)^4\right]^{3/2}. \quad (1)$$

Figure 2c shows the I_c vs V_g characteristics calculated from Eq. (1) for the same temperatures as in panel b. In the calculations we used the values for T_c and V_g^c determined from the experiment. Although definitely not conclusive and rather idealized, this theory is already able to grasp the essential features of our supercurrent FETs.

Figure 2d displays the I_c vs V_g characteristics measured at different temperatures of a square-shaped Ti transistor consisting of a $4\text{-}\mu\text{m}$ -long side, and the same film thickness. This structure was conceived to prove the effect also on a wide superconducting region with lateral dimensions largely exceeding λ_L and ξ_0 . The curves reveal a similar field-effect-induced I_c suppression though with reduced intensity with respect to the wires, as here only the back gate ($V_g \equiv V_b$) was applied. Yet, this result suggests that the relevant spatial scale is the one parallel to the applied electric field, in analogy to the Meissner-Ochsenfeld effect. Therefore, even in large but thin film structures ($t \ll \lambda_L, \xi_0$), I_c can be deeply affected by a perpendicular-to-plane electrostatic field.

We now discuss the joined impact of both electric and magnetic fields on the supercurrent in the wire. The perpendicular-to-plane magnetic field dependence of the FET critical current at 5mK and $V_g = 0$ is shown in Fig. 3a. Here we note the magnetic field-induced drop of I_c , and its full suppression at $\sim 127\text{mT}$. Furthermore, the fine structure visible on the non-monotonic $I_c(B)$ characteristic might be ascribed to the penetration of Abrikosov vortices in the Ti film upon increasing B [18]. The full I_c dependence on V_g for several magnetic fields at 5mK is summarized in Fig. 3b. All the following characterizations were performed before any external magnetic field was applied to the transistors, unless explicitly stated. Similarly to temperature, the effect is almost bipolar in V_g , and by increasing B leads to a widening of the I_c plateau. In addition, the threshold voltage V_g^c turns out to be weakly dependent on B , in contrast to its temperature independence (see Fig. 2b). The reason for this different behavior is still not understood. We note how sizable is the effect of the electric field on I_c even in the presence of magnetic fields approaching the critical one. Yet, our model still provides a reasonable description of the experiment, as shown in Fig. 3c (see SI for details).

Finally, quantification of the spatial extension of the electric field-induced non-local effect in the superconductor at 5mK and $B = 0$ is provided in Fig. 3d where the I_c suppression parameter (\mathcal{S}), defined as $\mathcal{S} = 100 \times [I_c(V_{si} = 0) - I_c(V_{si} = 90\text{V})]/I_c(V_{si} = 0)$ (with $i = 1, 2$, see the inset of panel d displaying a representative Ti comb-like device) whilst keeping the back gate voltage fixed at $V_b = 45\text{V}$, is shown. Differing from Figs. 2a,b and 3b, a higher $V_{si} = 90\text{V}$ gate voltage value was set to provide sizable supercurrent suppression via

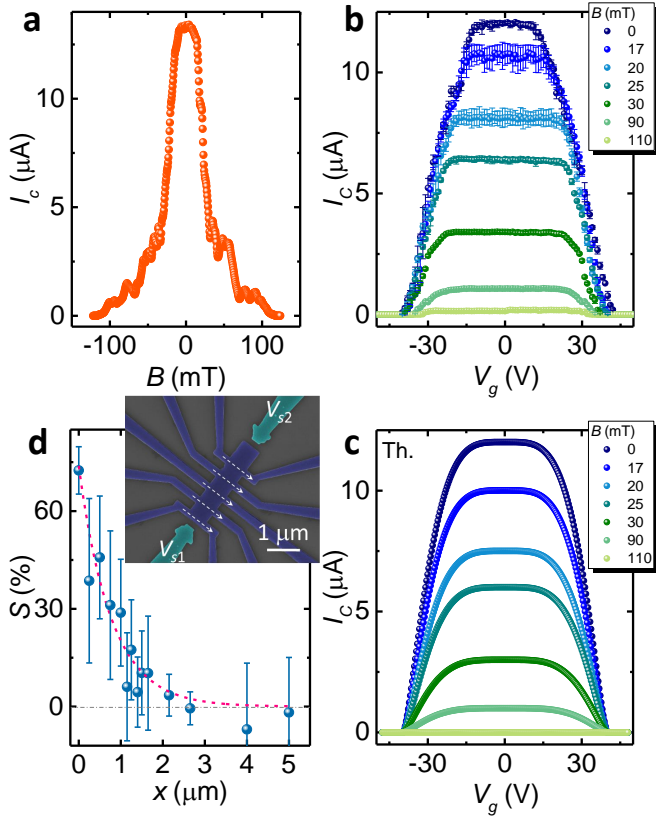


FIG. 3. Magnetic-field dependence of the FET, and spatial extension of the electric field-induced I_c suppression effect. **a**, Typical pattern of the critical current I_c vs perpendicular-to-plane magnetic field B measured at 5mK for $V_g = 0$. **b**, Behavior of I_c vs V_g measured at 5mK for several values of the perpendicular magnetic field. **c**, Theoretical critical current I_c vs V_g characteristics calculated at 5mK for the same values of magnetic field as in panel **b**. **d**, The inset shows a pseudo-color scanning electron micrograph of a typical Ti comb-like FET used to investigate the spatial extension of the electric field-induced I_c suppression effect in the superconducting film. White dashed arrows indicate the direction of the critical current measured in each wire composing the comb. The on-purpose asymmetry of device geometry allows to use the same wire for two I_c measurements at different distances from the side gates. The main panel displays the critical current suppression parameter (S) vs distance x measured at 5mK for $B = 0$. The suppression parameter represents the relative I_c reduction for $V_g = 90$ V with respect to zero applied side gate voltage, so that $S = 0$ indicates the absence of field-effect induced suppression of the critical current. x represents the average distance of the center of each wire from the lateral edges of the comb. The critical current of each wire is recorded by polarizing one side gate at the time (i.e., $V_{s1} \neq 0$ or $V_{s2} \neq 0$) while keeping the back gate voltage fixed at $V_b = 45$ V. The plot summarizes all S values measured in two different comb-like FETs having an average distance of 500nm and 1 μ m between the superconducting wires. Dashed line is an exponential damping fit to the data [$S(x) = S_0 \exp(-x/\lambda)$] with a decay length $\lambda \simeq 770 \pm 150$ nm. The error bars in panel **b** and **d** represent the standard deviation of the critical current I_c and S , respectively, calculated over 50 measurements.

a single side gate. S was determined for each wire composing the comb-like Ti FET designed on-purpose, and it is plot-

ted vs the distance (x) between the center of each wire and the lateral edges of the comb. A clear and substantial fading of field effect-induced suppression of I_c is observed by increasing the distance. Dashed line is an exponential decay fit to the data from which we extract an attenuation length $\lambda \simeq 770 \pm 150$ nm. This is intriguingly in reasonable agreement with the London penetration depth $\lambda_L \sim 900$ nm previously estimated in our Ti films. Furthermore, measurements of λ at different bath temperatures reveal that it is almost constant within the experimental error up to $\sim 80\%$ of T_c , then rapidly decreasing and vanishing by approaching the critical temperature (see SI). The above results on the spatial extension of the field-induced non-local effect contribute to further exclude a direct heat injection into the wire at the origin of supercurrent suppression since the typical thermal relaxation length in superconductors at low temperatures is of the order of tens of microns [19].

Our results on supercurrent FETs reveal the significant bipolar impact of a static electric field on a BCS superconducting film. Our physical interpretation points in the direction of a spatial deformation of the Cooper pairing parameter driven by electric fields localized at the surface of the superconductor by conventional screening. This yields a reduction of the available net wire section able to carry a supercurrent flow. A further step towards the understanding of the above effects might come from a set of complementary experiments, such as probing the superconductor density of states through tunneling spectroscopy, or investigating the phase rigidity by means of interference in SQUIDs, and the kinetic inductance in RF-based experiments. These findings represent a tool to envision superconducting field-effect devices ranging from tunable Josephson weak-links [8, 9] or interferometers [20–22] to Coulombic [23, 24] and coherent caloritronic structures [25, 26] as well as single-photon detectors [27, 28], which would benefit of field effect control to enhance their functionality. Given the general nature of our discovery which seems intrinsic to metallic superconducting thin films, there is flexibility for the optimization of this method both from the technological and material point of view. On the one hand, improved gating schemes exploiting thinner insulators could enable the reduction of gate voltage amplitudes by more than one order of magnitude. On the other hand, alternative superconductors such as thin NbN films ($t < 10$ nm) with T_c larger than 10K, and London penetration depth approaching 500nm [29, 30] might be suitable candidates for the implementation of an all-metallic high-speed superconducting field-effect electronics.

METHODS SUMMARY

Fabrication details and experimental set-up

The supercurrent FETs were fabricated with electron-beam lithography, and evaporation of metal through a resist mask onto a SiO_2/p^{++} -Si commercial wafer. The deposition of Ti

was performed at room temperature in an ultra-high vacuum electron-beam evaporator with a base pressure of $\sim 10^{-10}$ Torr at a deposition rate of $\simeq 11 - 13 \text{ \AA/s}$, whereas the deposition of Al at a deposition rate of $\simeq 1.5 \text{ \AA/s}$.

The magneto-electric characterization of the FETs was performed in a filtered He³-He⁴ dry dilution refrigerator at different bath temperatures down to 5 mK using a standard 4-wire technique. The current vs voltage characteristics of the FETs were obtained by applying a low-noise biasing current, with voltage across the superconducting nanowire being measured by a room-temperature battery-powered differential preamplifier. Gate biasing was provided by a low-noise voltage source whereas a low-frequency lock-in technique was used either for resistance vs temperature or resistance vs magnetic field measurements.

The data that support the plots within this paper and other findings of this study are available from the corresponding author upon reasonable request.

ACKNOWLEDGEMENTS

The authors wish to thank J. E. Hirsch for fruitful comments, and for having drawn the attention to relevant questions on key issues related to superconductivity so far considered well established. A. Braggio is acknowledged for a careful reading of the manuscript and for fruitful comments. J. S. Moodera, A. Shanenko, and P. Virtanen are acknowledged for useful discussions. The European Research Council under the European Unions Seventh Framework Program (FP7/2007-2013)/ERC Grant agreement No. 615187-COMANCHE, and MIUR-FIRB2013 Project Coca (Grant No. RBFR1379UX) are acknowledged for partial financial support. The work of G.D.S. and F.P. was funded by Tuscany Region under the FARFAS 2014 project SCIADRO. The work of E.S. was partially funded by the Marie Curie Individual Fellowship MSCAIFEF-ST No. 660532-SuperMag. P.S. has received funding from the European Union FP7/2007-2013 under REA Grant agreement No. 630925-COHEAT.

AUTHOR CONTRIBUTIONS

G.D.S. and F.P. fabricated the samples, and performed the measurements with E. S. G.D.S. and F.P. analyzed the experimental data with input from E.S. and F.G. P.S. developed the theoretical model with input from F.G., and performed the numerical calculations. F.G. conceived the experiment on field effect, and wrote the manuscript with input from all authors. All authors discussed the results and their implications equally at all stages.

COMPETING FINANCIAL INTERESTS

The authors declare no competing financial interests.

* francesco.giazotto@sns.it

- [1] London, F. & London, H. The Electromagnetic Equations of the Superconductor. *Proc. Roy. Soc. A* **149**, 71-88 (1935).
- [2] Hirsch, J. E., Charge expulsion and electric field in superconductors. *Phys. Rev. B* **68**, 184502 (2003).
- [3] Hirsch, J. E., Electrodynamics of superconductors. *Phys. Rev. B* **69**, 214515 (2004).
- [4] Tinkham, M. *Introduction to Superconductivity* (McGraw-Hill, 1996).
- [5] Tao, R., Xu, X., Lan, Y. C. & Shroyanagi, Y. Electric-field induced low temperature superconducting granular balls. *Physica C* **377**, 357-361 (2002).
- [6] Glover, R. E. III & Sherrill, M. D. Changes in Superconducting Critical Temperature Produced by Electrostatic Charging, *Phys. Rev. Lett.* **5**, 248-250 (1960).
- [7] Moro, R., Xu, X., Yin, S. & de Heer, W. A. Ferroelectricity in Free Niobium Clusters. *Science* **23**, 1265 (2003).
- [8] Larsen, T. W. *et al.* Semiconductor-Nanowire-Based Superconducting Qubit. *Phys. Rev. Lett.* **115**, 127001 (2015).
- [9] Casparis, L. *et al.* Gateon Benchmarking and Two-Qubit Operations. *Phys. Rev. Lett.* **116**, 150505 (2016).
- [10] Courtois, H., Meschke, M., Peltonen, J. T. & Pekola, J. P. Origin of Hysteresis in a Proximity Josephson Junction. *Phys. Rev. Lett.* **101**, 067002 (2008).
- [11] Bardeen, J. Critical Fields and Currents in Superconductors. *Rev. Mod. Phys.* **34**, 667 (1962).
- [12] Anthore, A., Pothier, H. & Esteve, D. Density of States in a Superconductor Carrying a Supercurrent, *Phys. Rev. Lett.* **90**, 127001 (2003).
- [13] Takayanagi, H. & Kawakami, T. Superconducting Proximity Effect in the Native Inversion Layer on InAs. *Phys. Rev. Lett.* **54**, 2449-2452 (1985).
- [14] Kleinsasser, A. W., Jackson, T. N., McInturff, D., Rammo, F. & Pettit, G. D. Superconducting InGaAs junction field-effect transistors with Nb electrodes. *Appl. Phys. Lett.* **55**, 1909-1911 (1989).
- [15] Doh, Y.-J. *et al.* Tunable Supercurrent Through Semiconductor Nanowires. *Science* **309**, 272-275 (2005).
- [16] Xiang, J., Vidan, A., Tinkham, M., Westervelt, R. M. & Lieber, C. M. Ge/Si mesoscopic Josephson junctions. *Nat. Nanotechnol.* **1**, 208-213 (2006).
- [17] Ginzburg, V. L. & Landau, L. D. On the theory of superconductivity. *Zh. Eksp. Teor. Fiz.* **20**, 35 (1950).
- [18] Morgan-Wall, T., Leith, B., Hartman, N., Rahman, A. & Marconi, N. Measurement of Critical Currents of Superconducting Aluminum Nanowires in External Magnetic Fields: Evidence for a Weber Blockade. *Phys. Rev. Lett.* **114**, 077002 (2015).
- [19] Fornieri, F., Timossi, G., Virtanen, P., Solinas, P. & Giazotto, F. $0 - \pi$ phase-controllable thermal Josephson junction. *Nat. Nanotechnol.* **12**, 425-429 (2017).
- [20] Clarke, J. & Braginski, A. I. (eds) *The SQUID Handbook* (Wiley-VCH, 2004).
- [21] Ronzani, A., Altimiras, C. & Giazotto, F. Highly sensitive superconducting quantum-interference proximity transistor. *Phys. Rev. Appl.* **2**, 024005 (2014).
- [22] Strambini, E. *et al.* The ω -SQUIPT as a tool to phase-engineer Josephson topological materials. *Nat. Nanotechnol.* **11**, 1055-1059 (2016).
- [23] Grabert, H. & Devoret, M. (eds) *Single Charge Tunneling: Coulomb Blockade Phenomena in Nanostructures* Ch. 1 (Springer, 1992).

- [24] Pekola, J. P., Giazotto, F. & Saira, O.-P. Radio-frequency single-electron refrigerator. *Phys. Rev. Lett.* **98**, 037201 (2007).
- [25] Fornieri, A. & Giazotto, F. Towards phase-coherent caloritronics in superconducting circuits. *Nat. Nanotechnol.* **12**, 944-952 (2017).
- [26] Martínez-Pérez, M. J., Solinas, P. & Giazotto, F. Coherent caloritronics in Josephson-based nanocircuits. *J. Low Temp. Phys.* **175**, 813-837 (2014).
- [27] Gol'tsman, G. N. *et al.* Picosecond superconducting single-photon optical detector. *Appl. Phys. Lett.* **79**, 705-707 (2001).
- [28] Giazotto, F. *et al.* Ultrasensitive proximity Josephson sensor with kinetic inductance readout. *Appl. Phys. Lett.* **92**, 162507 (2008).
- [29] Kamlapure, A. *et al.* Measurement of magnetic penetration depth and superconducting energy gap in very thin epitaxial NbN films. *Appl. Phys. Lett.* **96**, 072509 (2010).
- [30] Shapoval, T. *et al.* Quantitative assessment of pinning forces and magnetic penetration depth in NbN thin films from complementary magnetic force microscopy and transport measurements. *Phys. Rev. B* **83**, 214517 (2011).

SUPPLEMENTARY INFORMATION

Temperature dependence of electrostatic field attenuation length λ in Ti FETs

We have also measured the suppression parameter \mathcal{S} as a function of distance x at different bath temperatures in a comb-like Ti FET having an average distance of 500nm between the superconducting wires. For each temperature, an exponential decay fit to the $\mathcal{S}(x)$ data allowed to extract the corresponding attenuation length λ . The result of this procedure is shown in Fig. 4 which displays the measured $\lambda(T)$ curve. Specifically, we note the substantial temperature *independence* of the electrostatic field attenuation length up to ~ 330 mK, which corresponds to about 80% of the critical temperature of the Ti film composing the comb-like transistor ($T_c \sim 430$ mK). A further increase of the temperature above 330mK yields a rapid decay of λ , up to its full quenching around 375mK.

Aluminum (Al) supercurrent FETs

Analogous results for field effect-induced suppression of the critical current were observed in FETs made of aluminum (Al). In particular, the Al FETs consist of a wire of length $l = 800$ nm, width $w = 30$ nm, and thickness $t = 11$ nm. The Al FETs were realized without side gates so that only a back gate voltage V_b is used to control the supercurrent flow in the wire. From the normal-state resistance of the wire, $R_N \simeq 320\Omega$, and critical temperature, $T_c \simeq 1.5$ K, we deduce the London penetration length $\lambda_L \simeq 310$ nm, and the superconducting coherence length $\xi_0 \simeq 63$ nm assuming $\mathcal{N}_F = 2.15 \times 10^{47} \text{J}^{-1} \text{m}^{-3}$ for the density of states at the Fermi energy of our Al films. For these wires holds as well the condition $w, t \ll \lambda_L$ so that substantial modulation of the critical current is expected under the application of a static electric field.

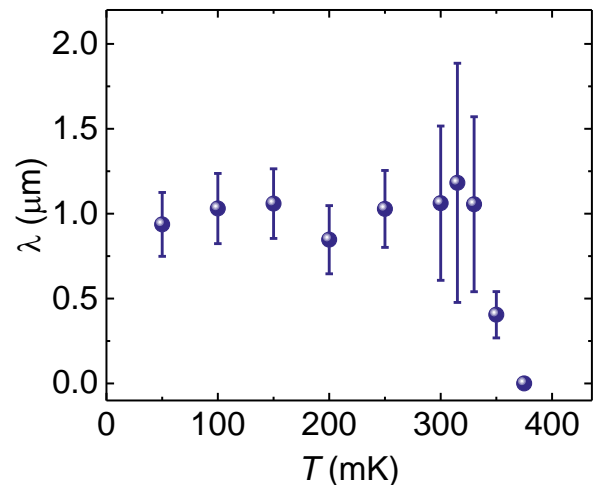


FIG. 4. **Temperature dependence of the electrostatic field attenuation length λ .** Behavior of λ vs T measured in a Ti comb-like FET having an average distance of 500nm between the superconducting wires. A critical temperature $T_c \simeq 430$ mK characterizes the Ti film realizing this transistor. λ is almost temperature independent up to ~ 330 mK, and then rapidly decays to zero by approaching T_c .

Figure 5a shows the wire current vs voltage ($I - V$) characteristics recorded at 5mK of bath temperature for several values of the applied gate voltage with $V_g \equiv V_b$. In the present case of Al thin film transistors, the switching critical current at zero gate voltage obtains values as high as $I_c \simeq 12.3\mu\text{A}$, which is reduced down to $\sim 8\mu\text{A}$ for $V_g = 70$ V corresponding to a relative suppression of the order of $\sim 35\%$. Similarly to Ti supercurrent FETs, the current-voltage characteristics show a clear hysteretic behavior but with a larger retrapping current. The electric field does not affect the $I - V$ characteristics when the wire switches into the normal state. Furthermore, differently from I_c , the retrapping current is unaffected by V_g . For the Al FETs it was not possible to totally quench I_c within the explored values of V_g .

The full temperature dependence of field-effect in the Al wire is displayed in Fig. 5b where the I_c vs V_g characteristics are shown for a few selected bath temperatures. In particular, a monotonic suppression of I_c occurs for $V_g \gtrsim 35$ V at temperatures below 100mK. At higher temperature, the threshold voltage for I_c suppression moves towards larger values while at the same time the critical current reduction turns out to be somewhat limited. In the investigated range of gate voltage, field-effect in these Al transistors persists up to ~ 600 mK, i.e., around 40% of critical temperature. The reduced impact of electric field on I_c might be correlated to the smaller λ_L (and ξ_0) characterizing these Al FETs in comparison to that obtained in Ti films.

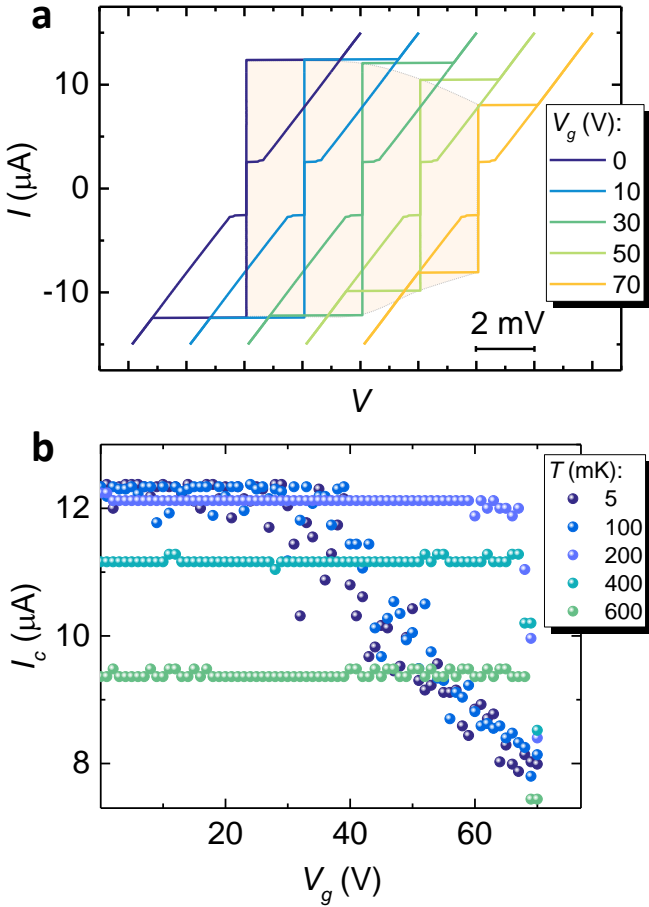


FIG. 5. Electrostatic field dependence of the Al supercurrent FET characteristics. **a**, Current-voltage ($I-V$) characteristics of an Al supercurrent FET measured at 5 mK for several values of the applied gate voltage ($V_g \equiv V_b$). Hatched area is a guide to the eye emphasizing the monotonic suppression of the critical current I_c by increasing V_g . Similarly to Ti superconducting FETs, when the supercurrent vanishes the Al FET $I(V)$ characteristics coincide with that in the normal state, independently of the applied voltage. The curves are horizontally offset for clarity. **b**, Behavior of the transistor critical current I_c vs V_g measured at different bath temperatures T . Note the monotonic suppression of I_c occurring for $V_g \gtrsim 35$ V at temperatures below 100 mK. This threshold voltage for supercurrent suppression largely increases at higher bath temperature.

Independence of the substrate on FETs performance, leakage current and leakage power

To exclude that the type of substrate has some role in the origin of the observed field effect we have also fabricated Ti supercurrent transistors on Si wafers produced by different manufacturers (both doped and undoped), and on sapphire substrates. Figure 6 displays in the top panels the I_c vs V_g characteristics recorded at 32 mK of bath temperature of a similar Ti FET deposited onto a SiO_2 wafer (panel a), and onto a sapphire substrate (panel b). Both FETs lack the backgate so that only side gates were used to control the supercurrent. In particular, besides the difference in the maximum critical cur-

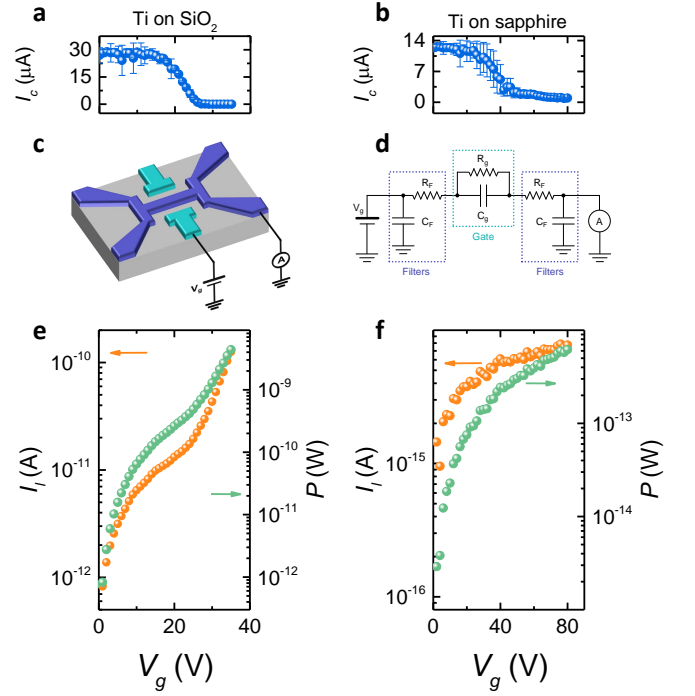


FIG. 6. Results obtained on FETs realized on different substrates, leakage current and leakage power. **a**, I_c vs V_g characteristic measured at 32 mK of bath temperature of a similar Ti FET fabricated on a different SiO_2 substrate. **b**, The same as in panel a but for a Ti FET fabricated on a sapphire substrate. The two devices show somewhat similar behavior which resembles that one of the Ti FET described in the main text of the paper. **c**, Scheme of the measurement setup used to characterize the leakage currents I_l . **d**, Complete equivalent electrical circuit of the setup used for the measurement of I_l vs V_g . C_F and R_F are the capacitor and the resistor used for the RF filtering of the cryostat, respectively. C_g and R_g are the effective capacitance and resistance between the gates and the wire, respectively. **e**, Leakage current I_l vs V_g (left vertical axis, orange dots), and corresponding leakage power P vs V_g (right vertical axis, green dots) for the same device of panel a. **f** The same as in panel e but for the FET fabricated on sapphire substrate shown in panel b. The error bars in panel a and b represent the standard deviation of the critical current I_c calculated over 50 measurements.

rent at zero gate bias, both FETs show the usual monotonic suppression of I_c by increasing V_g . The slightly different characteristics as a function of V_g stems from differences existing in the exact geometry of the two transistors. The comparison of the behavior of the Ti FETs shown in panels a and b of Fig. 6, and the one displayed in the main text of the paper confirms that the observed field effect is completely *independent* of the type of substrate used to realize the supercurrent transistors.

In addition, in characterizing the FETs we have measured the existing leakage current (I_l) present in the whole measurement circuit upon biasing the transistor gates, in order to assess the corresponding leakage power. Left vertical axes of Fig. 6 c and d show the I_l vs V_g characteristics (orange dots) of the transistors of panel a and b, respectively. Specifically, I_l obtains values as large as a few $\sim 10^{-11}$ A in the region of su-

percurrent suppression for FETs realized on SiO₂, whereas of the order of several $\sim 10^{-15}$ A for supercurrent transistors realized on sapphire substrates. The above values are standard leakage currents measured in all the devices we realized on different substrates. From this follows that in the former case I_l is typically around $\sim 10^{-6}I_c(V_g = 0)$ while for the latter the typical leakage current is around $\sim 10^{-10}I_c(V_g = 0)$.

The corresponding leakage power in the whole circuit due to losses, i.e., $P = I_l V_g$, is displayed in panels c and d for both transistors as green dots (right vertical axes). In particular, the typical maximum leakage power P for FETs realized onto SiO₂ is of the order of a few $\sim 10^{-10}$ W at complete supercurrent suppression (panel c) whereas it obtains values as large as a few 10^{-13} W in the same regime for FETs fabricated on sapphire (panel d).

We finally wish to emphasize that the above leakage power cannot be considered at the origin of supercurrent suppression in our FETs stemming from quasiparticle overheating due to direct injection of electric current. As a matter of fact, it can be shown through numerical calculations of the thermal steady-state of a superconductor under power injection that any quasiparticle overheating leading to a reduction or complete suppression of I_c would reflect into a sizable decrease of the wire critical temperature T_c . Measurements of critical temperature performed on different wires under V_g conditions leading to full suppression of I_c have shown that T_c is completely *independent* of gate voltage within the experimental error (see data in [1]), thereby supporting the above claim.

Phenomenological theory of field effect-induced suppression of the critical supercurrent I_c

In order to calculate the impact of the electric field on the critical current, we start from the superconducting free energy density F , which in the absence of magnetic field, reads [2–4]:

$$F = F_n + \alpha(T)|\psi|^2 + \frac{\beta}{2}|\psi|^4 + \frac{\hbar^2}{2m}|\nabla\psi|^2 + \Lambda \frac{\mathcal{E}_{tot}^2}{8\pi}. \quad (2)$$

Following Ginzburg-Landau theory, $\alpha = \alpha_0(T/T_c - 1)$ and β parameters describe the transition from superconducting to normal state. The superconducting state is obtained for $\alpha < 0$ and order parameter minimum is found for $\psi = \psi_0 = -\alpha/\beta$ [2, 3]. The term F_n represents the free energy density in the normal state, whereas the last term is the energy density associated to the total electric field \mathcal{E}_{tot} . The parameter Λ takes into account the penetration of the electric field into the superconductor; it can vary between $\Lambda = 0$ for no penetration and $\Lambda = 1$ for a fully penetrated superconductor. The value of Λ is presently unknown, and is supposed to be almost independent of ψ and $\nabla\psi$. From the experimental measurements we know that, while the critical current is strongly affected by the electric field, the wire critical temperature remains constant (see data in [1]). This poses a strong constraint on the phenomenological modelization within the Ginzburg-Landau

theory. The electric field cannot affect neither $|\psi|^2$ nor $|\psi|^4$ term in the free energy (2) since this would result in a change of the critical temperature [2, 3]. Therefore, the only way the electric field can affect the condensate is through the $\nabla\psi$ that describes the spatial deformation of the order parameter. The microscopic reason for such a condensate deformation is, at present, unknown. It could be due to the non-local propagation of the perturbation induced by surface electric fields or to the formation of inhomogeneous regions inside the superconductor. Below we show that such microscopic derivation is not essential within the framework of the Ginzburg-Landau theory, providing a simple phenomenological model able to catch the main features of the observed physical phenomenon and assuming a field dependent deformation of the order parameter.

We consider a wire with length d_x and lateral dimensions d_y and d_z (with $d_x \gg d_y, d_z$) and, accordingly, we set the coordinate axis (see Fig. 7). The current flows along the x direction and the extremes of the wire are at $y = \pm d_y/2$ and $z = \pm d_z/2$. The electric fields are applied along the y and z directions.

We write the order parameters as $\psi = \psi_x \psi_y \psi_z$. Along the current flowing direction ψ is uniform, i.e., $|\psi_x| = \psi_0 f$ where f is a space-independent parameter keeping into account the modulation of ψ . Our working assumption is that the presence of the electric field induces *deformation* the order parameter ψ along y and z directions. This deformation of ψ can be due either to a direct influence of the electric field inside the superconductor, or to the propagation of the electric perturbation occurring at the surface of the wire. To simplify the treatment, this deformation is described by Gaussian functions centered in $y = 0$ and $z = 0$, and with standard deviation σ_y and σ_z . Accordingly, we have

$$\psi = \psi_0 f \left(\frac{e^{-\frac{y^2}{2\sigma_y^2}}}{\sqrt{2\pi} \sigma_y/d_y} \right)^{\frac{1}{2}} \left(\frac{e^{-\frac{z^2}{2\sigma_z^2}}}{\sqrt{2\pi} \sigma_z/d_z} \right)^{\frac{1}{2}}. \quad (3)$$

An increase of the electric field \mathcal{E}_i along the i -th direction leads to a deformation of the order parameter along the same direction and to a decrease of σ_i . To describe this effect we assume that $\sigma_i = \mathcal{V}/\mathcal{E}_i$ where \mathcal{V} has the dimension of a voltage.

Keeping track of the spatial modulation of ψ , the free energy density (2) becomes

$$F = F_n + \alpha\psi^2 + \frac{\beta}{2}\psi^4 + \frac{\hbar^2}{8m} \left(\frac{y^2}{\sigma_y^4} + \frac{z^2}{\sigma_z^4} \right) \psi^2 + \Lambda \frac{\mathcal{E}_{tot}^2}{8\pi}. \quad (4)$$

By minimizing the latter with respect to ψ , the electric field contribution vanishes and we arrive at the equation $\alpha + \beta\psi^2 + \frac{\hbar^2}{8m} \left(\frac{y^2}{\sigma_y^4} + \frac{z^2}{\sigma_z^4} \right) = 0$. Using the relations $\alpha = -|\alpha|$ and $\psi_0 = |\alpha|/\beta$, we obtain

$$-|\alpha|(1 - f^2\psi_y^2\psi_z^2) = \frac{\hbar^2}{8m} \left(\frac{y^2}{\sigma_y^4} + \frac{z^2}{\sigma_z^4} \right). \quad (5)$$

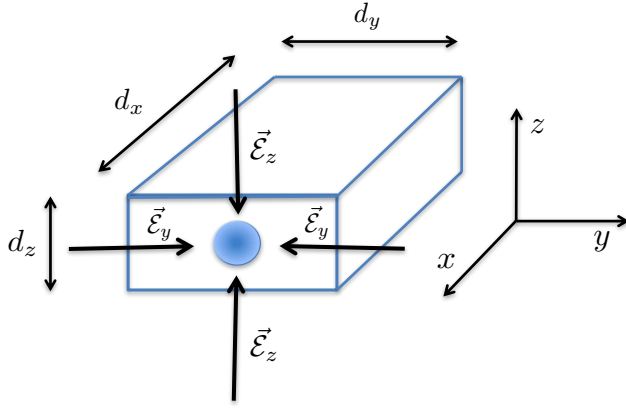


FIG. 7. **Effect of electric fields on a superconducting wire.** A superconducting wire of length d_x , d_y and d_z is subject to electric fields \vec{E}_y and \vec{E}_z . The electric fields produce a deformation of the Ginzburg-Landau order parameter (shown as a blue circle) along the field directions. The current flows along the x direction.

We take the average over y and z directions, i.e., $1/d_y \int_{-d_y/2}^{d_y/2} dy$ and $1/d_z \int_{-d_z/2}^{d_z/2} dz$. When the order parameter is strongly suppressed, i.e., for $\sigma_i \ll d_i$, we have that $1/d_y \int_{-d_y/2}^{d_y/2} \psi_y^2 dy \approx 1/d_y \int_{-\infty}^{\infty} \psi_y^2 dy = 1$ and $1/d_y \int_{-d_y/2}^{d_y/2} y^2 dy = d_y^2/12$ and analogously for the z coordinate.

For a symmetric wire, and equal applied electric fields we have $d_y = d_z = d$, $\mathcal{E}_y = \mathcal{E}_z = \mathcal{E}$, $\sigma_y = \sigma_z = \sigma$ and $f^2 = 1 - \frac{\hbar^2}{48m|\alpha|} \frac{d^2}{\sigma^4}$ that can be written as

$$f^2 = 1 - \frac{1}{\bar{\alpha}(T)} \left(\frac{\mathcal{E}}{\mathcal{E}_c} \right)^4 \quad (6)$$

where we have supposed that $\sigma = \mathcal{V}/\mathcal{E}$, and defined $\bar{\alpha}(T) = |\alpha(T)|/\alpha_0 = (T_c - T)/T_c$ and $\alpha_0 \equiv \alpha(T = 0)$ that has the dimension of an energy.

In equation (6) we have introduced an electric critical field $\mathcal{E}_c = [48m\alpha_0 V^4 / (\hbar^2 d^2)]^{1/4}$. Since $0 \leq \psi \leq \psi_0$, we have that $0 \leq f \leq 1$. Equation (6) tells us that if $\mathcal{E} \geq \bar{\alpha}^{1/4} \mathcal{E}_c$, the superconducting state is destroyed since there is no f that can satisfy it [2, 5].

The electric field \mathcal{E} in Eq. (6) is the *effective* field affecting the superconductor and generating the order parameter deformation. This could be different from the externally applied electric field \mathcal{E}_{ext} ; for this reason we take $\mathcal{E} = \chi \mathcal{E}_{ext}$.

It is natural to assume that χ depends on temperature. At $T = 0$ we assume that $\chi(T = 0) = 1$ and $\mathcal{E} = \mathcal{E}_{ext}$. At the superconducting critical temperature, the system becomes normal, and the external electric field has no effect on the metal. Therefore, we have $\chi(T = T_c) = 0$ and $\mathcal{E} = 0$. With these observations, we assume a temperature dependence of χ as follows:

$$\chi(T) = \left(1 - \frac{T}{T_c} \right)^\eta = \bar{\alpha}^\eta, \quad (7)$$

and we obtain a modified equation for f

$$f^2 = 1 - \frac{1}{\bar{\alpha}^{1-4\eta}} \left(\frac{\mathcal{E}_{ext}}{\mathcal{E}_c} \right)^4. \quad (8)$$

From Eq. (8), we can infer a phenomenological behavior of the critical current. In the absence of magnetic and electric fields, the critical current reads $I_c = \frac{8}{3\sqrt{3}} \frac{e}{\sqrt{m}\beta} |\alpha|^{3/2}$ [2, 3]. The information about the suppression of superconductivity can be included by modifying the critical current [normalized to $I_c^0 \equiv I_c(T = 0, \mathcal{E} = 0)$] as

$$\begin{aligned} \frac{I_c}{I_c^0} &= \bar{\alpha}^{3/2} f^{2\gamma} \\ &= \left(1 - \frac{T}{T_c} \right)^{3/2} \left[1 - \frac{1}{(1 - T/T_c)^{1-4\eta}} \left(\frac{\mathcal{E}_{ext}}{\mathcal{E}_c} \right)^4 \right]^\gamma \end{aligned} \quad (9)$$

where η and γ are parameters to be determined from the experiment. We can rewrite the critical current expression as a function of a critical voltage (V_g^c) with $\mathcal{E}_{ext}/\mathcal{E}_c = V_g/V_g^c$. The plots in Fig. 2c of the main text are obtained for $\eta = 1/4$ and $\gamma = 3/2$.

Critical current with electric and magnetic field

The description of the critical current behaviour in presence of both electric \mathcal{E} and magnetic field B is more complex. It is known that the presence of a magnetic field reduces the critical current and the standard theory predicts a decrease with B (see Refs. [2, 3, 5–7]).

However, as shown in Fig. 3a of the main text, the experimental measured values of the critical current at $\mathcal{E} = 0$ have a complex dependence on B . In particular the oscillator behavior at high magnetic field, are related to the Weber blockade [8] that is not accounted in the standard theory [2, 5–7]. For this reason, here we adopt a more practical approach.

From the previous discussion we know that the critical current is suppressed as $(\mathcal{E}_{ext}/\mathcal{E}_c)^4$. To include the magnetic field dependence, we use the phenomenological function

$$\frac{I_c}{I_c^0} = I_{meas}(B) \left[1 - \left(\frac{\mathcal{E}_{ext}}{\mathcal{E}_c} \right)^4 \right]^\gamma = I(B) \left[1 - \left(\frac{V_g}{V_g^c} \right)^4 \right]^\gamma \quad (10)$$

where $I_{meas}(B) \equiv I_{meas}(B, \mathcal{E} = 0)$ is the (normalized) value of the critical current measured at B and $\mathcal{E} = 0$. Since the measurements are done at constant and low temperature ($T = 10$ mK corresponding to $T/T_c = 0.03$), we can assume $\bar{\alpha} \approx 1$. The plots in Fig. 3d of the main text are obtained from Eq. (10) with $\gamma = 3/2$.

Supplementary Information References

* francesco.giazotto@sns.it

- [1] Paolucci, F., De Simoni, G., Strambini, E., Solinas, P. & Gi-azotto, F. Ultra-efficient superconducting Dayem bridge field-effect transistor. arXiv:1803.04925.
- [2] de Gennes, P. G. *Superconductivity of Metals and Alloys*, Advanced Books Classics (Westview Press, 1999).
- [3] Tinkham, M. *Introduction to Superconductivity* (McGraw-Hill, 1996).
- [4] Ginzburg, V. L. & Landau, L. D. On the theory of superconductivity. *Zh. Eksp. Teor. Fiz.* **20**, 35 (1950).
- [5] Schmidt, V., Müller, P & Ustinov, A., *The Physics of Superconductors: Introduction to Fundamentals and Applications* (Springer, 1997)
- [6] Bardeen, J. Critical Fields and Currents in Superconductors. *Rev. Mod. Phys.* **34**, 667 (1962).
- [7] Mydosh, J. A. & Meissner, H. Dependence of the Critical Currents in Superconducting Films on Applied Magnetic Field and Temperature. *Phys. Rev.* **140**, A1568 (1965).
- [8] Morgan-Wall, T., Leith, B., Hartman, N., Rahman, A. & Marković, N. Measurement of Critical Currents of Superconducting Aluminum Nanowires in External Magnetic Fields: Evidence for a Weber Blockade. *Phys. Rev. Lett.* **114**, 077002 (2015).